Effect of electronic angular momentum exchange on photoelectron anisotropy following the two-color ionization of krypton atoms

N. Saquet, D. M. P. Holland, S. T. Pratt, D. Cubaynes, X. Tang, G. A. Garcia, L. Nahon, and K. L. Reid

Effect of electronic angular momentum exchange on photoelectron anisotropy following the two-colour ionization of krypton atoms

N. Saquet,[a] D.M.P. Holland,[b] S.T. Pratt,[c] D. Cubaynes,[d,e] X. Tang,[e,f] G. A. Garcia,[e] L. Nahon[e] and K.L. Reid[a]

a.   *School of Chemistry, University of Nottingham, Nottingham NG7 2RD, United Kingdom*

b.   *STFC, Daresbury Laboratory, Daresbury, Warrington, Cheshire WA4 4AD, United Kingdom*

c.   *Argonne National Laboratory, Argonne, IL 60439 USA*

d.   *Université Paris Sud, CNRS UMR 8214, ISMO, F-91405 Orsay, France*

e.   *Synchrotron Soleil, L'Orme des Merisiers, St Aubin BP 48, F-91192 Gif Sur Yvette, France*

f.   *Present address: Laboratory of Atmospheric Physico-Chemistry, Anhui Institute of Optics and Fine Mechanics, Chinese Academy of Sciences, Hefei, 230031 Anhui, China*

Abstract

We present photoelectron energy and angular distributions for resonant two-photon ionization via several low-lying Rydberg states of atomic Kr. The experiments were performed by using synchrotron radiation to pump the Rydberg states and a continuous wave laser to probe them. Photoelectron images, recorded with both linear and circular polarized pump and probe light, were obtained in coincidence with mass-analyzed Kr ions. The photoelectron angular distributions and branching ratios for direct ionization into the Kr^+ $^2P_{3/2}$ and $^2P_{1/2}$ spin-orbit continua show considerable dependence on the intermediate level, as well as on the polarizations of the pump and probe light. Photoelectron angular distributions were also recorded with several polarization combinations following two-colour excitation of the $(^2P_{1/2})5f[5/2]_2$ autoionizing resonance. These results are compared with the results of recent work on the corresponding autoionizing resonance in atomic Xe [E. V. Gryzlova et al. New J. Phys. **17**, 043054 (2015)].

1.   Introduction

Photoelectron angular distributions (PADs) have long been claimed as powerful probes of electronic structure.[1-3] This idea has been put to use in studies of photodetachment from anions,[4, 5] and elegantly exploited in femtosecond time-resolved photoelectron imaging studies of non-adiabatic dynamics in neutral molecules. [6-9]   Given this interest, there is a need for systematic studies of the variation of PADs with the electronic state of the neutral and the ion. It has been shown that (at least) partial alignment of molecular axes improves the sensitivity of the PAD to electronic character;

1

this alignment can be achieved through photoexcitation, through strong-field alignment methods, or through coincidence imaging.[6-11] In the atomic case, alignment of orbital angular momentum serves the same purpose as alignment of molecular axes, and a number of laser-based studies have shown that achieving this through photoexcitation prior to photoionization can lead to a PAD with exquisite sensitivity to the angular momentum composition of the intermediate state.[12-14] However, although systematic studies have been performed in which different intermediate electronic states are prepared, generally only a single ionic electronic state has been accessible in each case. Furthermore, these studies have generally been restricted, by available laser wavelengths, to atoms with relatively low-lying electronic states and ionization potentials.

A recent development has been in the use of light from short wavelength free electron lasers (FELs) to excite and ionize atoms and molecules. This enables the preparation of high-lying electronic states prior to photoionization, as well as the formation of multiple ion states, but as a consequence of the broad bandwidth associated with the short FEL pulses, superpositions of states are generally prepared.[15] An alternative is to combine the capabilities of narrow bandwidth "table-top" laser systems with those of synchrotron radiation (SR). This is challenging because the relatively low photon flux of the SR is not well suited to resonant multiphoton schemes, but the technique has been demonstrated in a few cases.[16-18] In a recent study of direct relevance to the one reported here, Meyer and coworkers have reported polarization-dependent PADs following the resonant photoionization of Xe atoms which were state-selected by SR and ionized by visible laser radiation.[19, 20] In their work, ionization was enhanced through the use of an autoionizing resonance, and only a single ionic state was energetically accessible.

In the present work, we adopt the same experimental scheme as that employed by Meyer and coworkers, but aim to study the influence of the spin-orbit state of both the neutral and the ion on the PADs observed from Kr atoms that have been excited with SR. This has been achieved by selecting a series of intermediate states that can be ionized to populate more than one ionic state. We have studied examples of both direct ionization and autoionization processes from neutral states with different selected angular momentum quantum numbers. In order to optimize the information content of our measurement, we have employed three different SR/laser polarization combinations.

2. Experimental

The experiments were performed at the vacuum ultra-violet (VUV) variable polarization beamline DESIRS,[21] of synchrotron SOLEIL, together with the molecular beam chamber SAPHIRS[22] and the DELICIOUS III double imaging particle coincidence spectrometer.[23] A supersonic beam of pure Kr, produced by expanding 1 bar of Kr through a 70 μm nozzle, was doubly skimmed and crossed with counter-propagating SR and laser beams, each of which could be linearly (LP), left-circularly (LCP) or right-circularly (RCP) polarized. The VUV light was used to prepare a series of intermediate electronic states which are listed in Table I.[24] In these experiments, we used a 200 l/mm grating and 50 μm exit slits to provide a moderate resolution of ~4 meV at 12 eV, with a photon flux of ~10^{12} photons/second. The SR photon energy was tuned to the intermediate resonances by monitoring the VUV fluorescence that reached the spectrometer's microchannel plates. The spectrometer's coincidence capability ensures that this signal does not interfere with the data acquisition (see below).

The excited atoms were subsequently ionized by light at ~595 nm produced by a continuous wave dye laser (Coherent) pumped by a frequency-doubled VERDI solid state laser (Coherent). The average laser power was ~1.4 W and the laser bandwidth was ~1.3 cm^{-1}. The SR/laser polarization combinations used were (LP,LP), (RCP,RCP) and (RCP,LCP). The SR polarization state was specified by the settings of the undulator, which had been calibrated by a dedicated in situ VUV polarimeter[25] located just upstream of the sample. In particular, in the Circularly Polarized Light (CPL) mode of operation, the absolute degree of circular polarization was >0.97. The helicity of the circularly polarized laser light could not be determined directly with our experimental arrangement. We have assumed that the photoelectron anisotropy parameters for Kr, measured in the region of the $(^2P_{1/2})5f[5/2]_2$ autoionizing resonance, should exhibit a similar trend to those measured and calculated for the corresponding $(^2P_{1/2})4f[5/2]_2$ resonance in Xe, and used this similarity to assign the helicity of the laser light. A more detailed discussion of this topic is given in section 4.

The ions and electrons resulting from the two-photon excitation/ionization process were accelerated in opposite directions perpendicular to the molecular and photon beams inside the DELICIOUS III spectrometer which combines a velocity map imaging (VMI) electron spectrometer and a modified Wiley McLaren imaging analyzer. The effective electric field in the interaction region was ~44.4 V/cm. This is expected to have a minimal effect on the present Rydberg states which have relatively low principal quantum number. The spectrometer was operated in coincidence mode, enabling photoelectron images associated with each Kr isotope to be acquired. This also enabled any electron signal not associated with the ionization of Kr atoms to be discarded. The typical

photoelectron kinetic energy resolution that can be achieved at the edge of the detector is about 3%.[22] The images were inverted using the pBasex software,[26] which provides both the photoelectron intensity and the angular distribution parameters as a function of the photoelectron kinetic energy. The pBasex method is applicable when the images have cylindrical symmetry. In the present experiments, the axis of cylindrical symmetry is defined by the polarization axis when linear polarized light is used, and by the light propagation direction when circular polarized light is used. We have not used mixed linear/circular polarizations, which would break the cylindrical symmetry of the experiment.
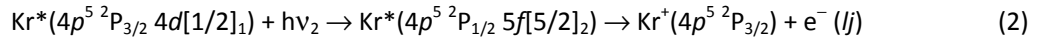
3. Results

The synchrotron radiation prepares the Kr atoms in excited states with defined angular momenta:
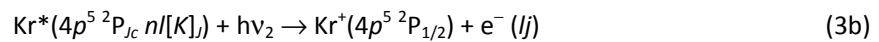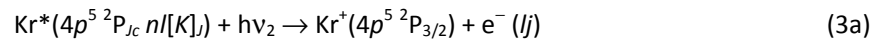
$$Kr(4p^6) + h\nu_1 \rightarrow Kr^*(4p^5 \, {}^2P_{Jc} \, nl[K]_J) \tag{1}$$
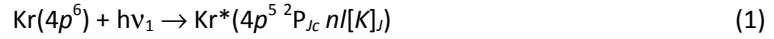
Here, the $J_c l$ coupling scheme has been used,[27] where J_c corresponds to the angular momentum of the ion core (${}^2P_{3/2}$ or ${}^2P_{1/2}$) and l corresponds to the orbital angular momentum of the Rydberg electron. The value of K (in square brackets) corresponds to the total angular momentum minus spin (i.e., $J_c + l$), and the total angular momentum J is given as the subscript to the square bracket. The excited states that were studied are listed in Table I.

Photoionization of the $({}^2P_{3/2})4d[1/2]_1$ state with laser light at ~595 nm accesses the $({}^2P_{1/2})5f[5/2]_2$ autoionizing resonance at 14.11758 eV (using the energy of 113866 cm^{-1} for the $({}^2P_{1/2})5f$ configuration[24]). This resonance can decay only into the Kr$^+$ ${}^2P_{3/2}$ continuum:

$$Kr^*(4p^5 \, {}^2P_{3/2} \, 4d[1/2]_1) + h\nu_2 \rightarrow Kr^*(4p^5 \, {}^2P_{1/2} \, 5f[5/2]_2) \rightarrow Kr^+(4p^5 \, {}^2P_{3/2}) + e^- \, (lj) \tag{2}$$

By contrast, using the same probe wavelength to photoionize the remaining four intermediate states listed in Table I provides sufficient energy to populate both the ${}^2P_{3/2}$ ground state and the ${}^2P_{1/2}$ spin-orbit excited state of the ion:

$$Kr^*(4p^5 \, {}^2P_{Jc} \, nl[K]_J) + h\nu_2 \rightarrow Kr^+(4p^5 \, {}^2P_{3/2}) + e^- \, (lj) \tag{3a}$$

$$Kr^*(4p^5 \, {}^2P_{Jc} \, nl[K]_J) + h\nu_2 \rightarrow Kr^+(4p^5 \, {}^2P_{1/2}) + e^- \, (lj) \tag{3b}$$

These spin-orbit states can be distinguished in the photoelectron images.

The photoelectron angular distributions (PADs) provide information on the angular momentum carried away by the photoelectron, and can be expressed in terms of anisotropy parameters, β_{LM}, according to the expression

$$I(\theta,\phi) = \beta_{00}Y_{00}(\theta,\phi) + \beta_{20}Y_{20}(\theta,\phi) + \beta_{40}Y_{40}(\theta,\phi),\qquad(4)$$

where the $Y_{LM}(\theta,\phi)$ are spherical harmonics and the expansion is limited by the number of photons involved and by the experimental symmetry.[2] The angle θ is measured with respect to the polarization axis in the case of the (LP,LP) geometry and with respect to the propagation axis in the case of the (RCP,RCP) and (RCP,LCP) geometries. In these experiments we maintain cylindrical symmetry for all polarization combinations and so we can rewrite Eq. (4) in the form

$$I(\theta) = c_0(1 + c_2P_2(\theta) + c_4P_4(\theta)),\qquad(5)$$

where the $P_L(\theta)$ are Legendre polynomials. In our experiments the c_L coefficients are determined by averaging values across the range of kinetic energies corresponding to the full-width half-maximum of each photoelectron peak that is observed.

The uncertainty in our measured c_L coefficients due to counting statistics is estimated as ~0.03 for the high intensity photoelectron peaks produced through direct ionization or by autoionization, and as ~0.1 to 0.2 for the lower intensity peaks formed via an indirectly populated intermediate state. Other potential sources of error, such as detector inhomogeneities, or those associated with the image inversion and analysis procedure, due, for example, with the choice of image centre and the determination of the resulting photoelectron peak width and kinetic energy, may contribute an additional uncertainty of ~0.05 to 0.1.

3.1 The (^{2}P$_{3/2}$)4d[1/2]$_1$ intermediate resonance and (^{2}P$_{1/2}$)5f[5/2]$_2$ autoionizing resonance

The study of the (^{2}P$_{3/2}$)4d[1/2]$_1$ intermediate state concentrated on how the PAD changed as different points across the profile of the autoionizing resonance were accessed by a selection of laser wavelengths, and as the relative polarization of the SR and laser light was varied. These results can then be compared with the exactly analogous two-colour results for Xe atoms obtained by Meyer and coworkers,[19] in which they pumped the Xe (^{2}P$_{3/2}$)5d[3/2]$_1$ state and probed the (^{2}P$_{1/2}$)4f[5/2]$_2$ autoionizing resonance. In Fig. 1 we show examples of photoelectron images recorded with (LP,LP), (RCP,LCP) and (RCP,RCP) polarization combinations, together with the corresponding

inverted images which have been processed such that only electrons measured in coincidence with the Kr isotopes with zero nuclear spin (masses 80, 82, 84, and 86) are included. In this Figure, we can see that a single ring (photoelectron peak) appears whose anisotropy depends on wavelength and on polarization geometry. This photoelectron peak results from the spin-orbit autoionization of the Kr $(^2P_{1/2})5f[5/2]_2$ state into the Kr$^+$ $^2P_{3/2}$ continuum with the ejection of an odd-l photoelectron. Comparison of the images shown in Figs. 1(c) and 1(d) reveals a noticeable difference in the images observed with left and right circularly polarized light; this difference is referred to as circular dichroism. Such an effect cannot occur in the photoionization of randomly orientated non-chiral targets but can be caused by an introduction of anisotropy,[28] as achieved by the excitation step in this case.

In Fig. 2 we show the behaviour of the c_2 and c_4 parameters as a function of the laser wavelength for the three different polarization combinations. The maximum of the autoionizing resonance profile corresponds to a laser wavelength of 595.920 nm (2.08055 eV). The plots in Figure 2 can be compared with the analogous plots for Xe presented in Ref. [20], which were seen to be isotope-dependent as a consequence of the depolarizing effect of non-zero nuclear spin.[29] For the present analysis, we have selected Kr isotopes with zero nuclear spin, and so no depolarizing effect can occur. For the (LP,LP) combination, the qualitative behaviour of the c_2 and c_4 parameters is broadly similar to that observed for the Xe isotopes with zero nuclear spin, showing a minimum on the red side of the autoionization profile. For the two circularly polarized combinations, some of the parameters vary across the resonance whilst others show little change and exhibit values similar to those determined off-resonance. The values of the c_L parameters at each wavelength are given in Table II. In the case of (LP,LP) the PADs evolve from peaking at 45° to the polarization axis to peaking along the polarization axis as the photon energy is increased. For (RCP,LCP) the PADs peak at 45° to the propagation axis, whilst those for (RCP,RCP) peak along the propagation axis, at all photon energies.

3.2 The $(^2P_{3/2}) 5d[1/2]_1$, $(^2P_{1/2})4d[3/2]_1$, $(^2P_{1/2})6s[1/2]_1$ and $(^2P_{3/2})5d[3/2]_1$ intermediate resonances

Two-colour photoelectron images were recorded for four higher energy bound state resonances accessed by the absorption of synchrotron radiation. For each of these resonances, which are listed in Table I, the absorption of a dye laser photon accesses a featureless continuum above both the $^2P_{3/2}$ and $^2P_{1/2}$ ionization thresholds.

In Fig. 3 we show an inverted photoelectron image, together with its extracted photoelectron spectrum and PADs, for ionization of the $(^2P_{3/2})5d[1/2]_1$ resonance in the (LP,LP) geometry. The equivalent photoelectron spectra and PADs for the (RCP,RCP) and (RCP,LCP) schemes are shown in Fig. 4, with the c_L parameters for all three polarization geometries listed in Table III. In all cases two rings with different anisotropies are observed in the photoelectron image, giving rise to a photoelectron spectrum with two peaks. These peaks correspond to the population of the two spin-orbit states of Kr^+, with the $^2P_{3/2}$ state at 13.9996 eV and the $^2P_{1/2}$ state at 14.6655 eV. Interestingly, the photoelectron peak corresponding to the $^2P_{1/2}$ state of the ion has significant intensity in all three polarization geometries, despite the fact that the formation of this state requires a change in the spin-orbit character of the core. The PADs (and hence c_L values) can be seen to depend strongly on both the ion spin-orbit state and the polarization geometry. For example, for linear polarization, the maximum photoelectron intensity is observed along the polarization axis for the $^2P_{1/2}$ state and at 45° to the polarization axis for the $^2P_{3/2}$ state. These observations are discussed further in Section 4.

Figure 5 shows the inverted photoelectron images for the ionization from the $(^2P_{1/2})4d[3/2]_1$, $(^2P_{1/2})6s[1/2]_1$ and $(^2P_{3/2})5d[3/2]_1$ intermediate states. Low collection statistics precluded the acquisition of data in all three polarization geometries for these resonances, and thus all of the images were recorded in the (LP,LP) geometry. The PADs extracted from these images depend strongly on the intermediate state that is ionized. All three images show not only the two rings expected for populating the $^2P_{3/2}$ and $^2P_{1/2}$ states of the ion, but also a number of additional rings. In particular, at least two additional rings are observed following ionization from the $(^2P_{1/2})4d[3/2]_1$ and $(^2P_{1/2})6s[1/2]_1$ states, and multiple rings are observed following ionization from the $(^2P_{3/2})5d[3/2]_1$ state. A possible explanation for the appearance of these extra rings is that the initially prepared level fluoresces and that the levels populated through this fluorescence are then ionized by a 595 nm photon from the laser beam. Such a mechanism has been observed before in the case of Xe atoms,[30] and is illustrated schematically in Fig. 6. This mechanism is discussed further in Section 4.

Polar plots of the PADs extracted from Fig. 5 are shown in Fig. 7, and the corresponding c_L parameters are listed in Table III, along with the spin-orbit branching ratios. The PADs corresponding to the $(^2P_{1/2})4d[3/2]_1$ and $(^2P_{1/2})6s[1/2]_1$ resonances show similar behaviour; in both cases formation of the $^2P_{3/2}$ ion state gives rise to a PAD that peaks at 45° to the polarization axis, whereas formation of the $^2P_{1/2}$ ion state gives rise to a PAD that peaks along the polarization axis.

The PADs corresponding to the $(^2P_{3/2})5d[3/2]_1$ state show different behaviour, with photoelectrons ejected most probably along the polarization axis for both Kr^+ spin-orbit states.

In Fig. 8, we show polar plots of photoelectron intensity following the ionization of each of the states populated by fluorescence. Each of these plots is labelled by an assigned fluorescing transition from the prepared intermediate state. These assignments are given in Table IV and are discussed further in Section 4. In all cases, subsequent absorption of the 595 nm photon is energetically constrained to populate only the $^2P_{3/2}$ ground state of Kr^+. Comparison of Figs. 7 and 8 shows that the PADs are less anisotropic following ionization of the fluorescently populated states than they are following ionization of the states that have been initially prepared. The anisotropies also depend on the fluorescing transition, as expected from the different angular momenta involved; this is discussed further in Section 4.

4. Discussion

4.1 Ionization dynamics: The $(^2P_{3/2})4d[1/2]_1 \rightarrow (^2P_{1/2})5f[5/2]_2$ autoionization

An extensive review of studies of the near-threshold ionization dynamics in rare gas atoms has been provided by Sukhorukov et al.[31] A quantitative description of the angular distributions observed here requires a knowledge of the radial dipole matrix elements and phases that describe the photoionization process,[20] and is beyond the scope of the work presented here. However, Gryzlova et al. have presented a formulation for the anisotropy parameters expected for the case in which the photoelectron wavefunction is dominated by channels with $J = 2$. The predictions from this formulation were consistent with the observations made for the Xe $(^2P_{1/2})4f[5/2]_2$ resonance, but quantitative agreement could only be achieved by considering both the resonant and nonresonant ionization signals.[20] We would expect the resulting equations also to be applicable to the peak of the Kr $(^2P_{1/2})5f[5/2]_2$ $J = 2$ autoionizing resonance studied here. In particular, for pure $J = 2$ continua, Gryzlova et al. give:[20]

$$c_2^{(LP,LP)} = c_2^{(RCP,LCP)} = -c_2^{(RCP,RCP)} \tag{6}$$

and

$$c_4^{(LP,LP)} = -c_4^{(RCP,LCP)} = 6c_4^{(RCP,RCP)} . \tag{7}$$

The values shown in Table II are not entirely consistent with Eqs. (6) and (7). This observation suggests that the nonresonant ionization background, and in particular the other allowed values of J, must be included to account for the observed angular distributions.

Although our measured values of c_2 and c_4 in the vicinity of the autoionizing resonance in Kr are not fully consistent with the calculated variations in these parameters for the corresponding resonance in Xe, there appear to be sufficient similarities to allow the helicity of the circularly polarized laser light used in our experiment to be assigned. In particular, with our choice of helicity our experimental value for c_2(LP,LP) is of similar magnitude but of opposite sign to that for the (RCP,RCP) polarization combination, as predicted,[20] and our value of c_4(LP,LP) is a factor of ~4 larger than c_4(RCP,RCP), again in reasonable accord with the predicted behaviour.

In the case of the (LP,LP) geometry, it can be seen in Figure 2 and Table II that the c_2 values vary between ~0.3 and 0.9 across the resonance; this variation is considerably smaller than that observed in Xe.[20] The change in the value of c_4 is more significant, ranging from ~0.0 at the peak of the resonance to ~-1.1 at the low energy wing of the profile. While the magnitude of this variation is similar to that observed in Xe, it has the opposite sign. We note that the asymmetry of the absorption cross section across the resonance in Kr has the opposite sign from that in Xe. In the (RCP,RCP) and (RCP,LCP) geometries, some of the c_2 and c_4 parameters exhibit variations across the resonance whilst others do not. The interpretation of these observations awaits more detailed theoretical calculations.

4.2 Ionization dynamics: Direct ionization of the (^{2}P$_{3/2}$) 5d[1/2]$_1$, (^{2}P$_{1/2}$)4d[3/2]$_1$, (^{2}P$_{1/2}$)6s[1/2]$_1$ and (^{2}P$_{3/2}$)5d[3/2]$_1$ states

The selection rules for preparation of the intermediate resonance require that $\Delta M_J = 0$ for LP and $\Delta M_J = +1$ for RCP. Because the total angular momentum quantum number, J, is 1 for all of the prepared intermediate resonances, only the $M_J = 0$ sub-level can be accessed with LP and only the $M_J = +1$ sub-level can be accessed with RCP. Therefore, with the absorption of the probe laser photon:

> Ionization in the (LP,LP) geometry results in $M_J = 0 \rightarrow 0$
>
> Ionization in the (RCP,RCP) geometry results in $M_J = +1 \rightarrow +2$
>
> Ionization in the (RCP,LCP) geometry results in $M_J = +1 \rightarrow 0$.

Assuming that the bound states have pure l character, the selection rules $\Delta l = \pm 1$ and $\Delta J = \pm 1$ also apply for (LP,LP) and (RCP,RCP) ionization, and $\Delta l = \pm 1$ and $\Delta J = 0, \pm 1$ for (RCP,LCP) ionization. Using these selection rules the photoionization continua that can be accessed for each resonance in each polarization scheme are listed in Table V. Through study of the direct ionization of these

resonances we can observe the effect of polarization geometry, core angular momentum, and orbital angular momentum on the resulting photoelectron spectra and PADs. The resulting anisotropy parameters and spin-orbit branching ratios are listed in Table III. The core-switching probabilities (i.e. the ion spin-orbit branching ratio) are also listed in Table III where they can be seen to vary from 0.2 to 0.7.

(a) Effect of polarization

Direct ionization via the $(^2P_{3/2})5d[1/2]_1$ state was studied in all three polarization geometries. The selection rules dictate that ionization of this state in the (RCP,RCP) geometry can only result in continua with $(J, M_J) = (2, +2)$, while ionization in the (LP,LP) geometry can result in $(J, M_J) = (0,0)$ or $(2,0)$, and ionization in the (RCP,LCP) geometry can result in $(J, M_J) = (0,0)$, $(1,0)$ or $(2,0)$. These requirements, along with the selection rule on l, lead to the allowed continua shown in Table V.

From Figs. 3 and 4 and Table III we can see that, for both spin-orbit states, ionization in the (LP,LP) and (RCP,LCP) geometries gives rise to PADs with a significant contribution from the $P_4(\cos\theta)$ term in Eq. (5), whereas the (RCP,RCP) geometry gives rise to PADs that are dominated by the $P_2(\cos\theta)$ term. The c_2 parameter changes sign from positive in the (LP,LP) geometry to negative in the two CP geometries. The most anisotropic PADs are seen in the (LP,LP) geometry, which also gives the highest core-switching probability, resulting in 70% of the ions being formed in the $^2P_{1/2}$ spin-orbit state. The lowest core switching probability and least anisotropic PADs occur in the (RCP,LCP) geometry in which 50% of the ions are formed in the $^2P_{1/2}$ spin-orbit state. It can be seen from Table V that in the (RCP,LCP) geometry there are more possible channels that result in a *p* wave photoelectron than an *f* wave photoelectron, particularly for the $^2P_{1/2}$ ion state, whereas in the (RCP,RCP) geometry there is an equal number of possible *p* wave and *f* wave channels. This gives a possible explanation for the relatively small c_4 values seen in the (RCP,LCP) geometry.

(b) Effect of l and J_c

Here we discuss the observed results in the (LP,LP) geometry for the four direct ionization processes. Two of the intermediate Rydberg states; $(^2P_{3/2})5d[1/2]_1$ and $(^2P_{3/2})5d[3/2]_1$, have $^2P_{3/2}$ ion cores, while the other two; $(^2P_{1/2})4d[3/2]_1$ and $(^2P_{1/2})6s[1/2]_1$, have $^2P_{1/2}$ ion cores. In the simplest approximation, photoionization of the intermediate state would be a single-electron transition, in which the Rydberg electron was excited into the continuum with the ion core acting as a spectator. However, while Table III shows that such core-preserving transitions dominate for the $(^2P_{1/2})4d[3/2]_1$ and $(^2P_{3/2})5d[3/2]_1$ states, both states also show significant propensity for core-switching transitions.

More dramatically, in the cases of the $(^2P_{3/2})5d[1/2]_1$ and $(^2P_{1/2})6s[1/2]_1$ states, the core-switching transition is actually more intense than the core-preserving process. We note in passing that the transition from the $(^2P_{3/2})4d[1/2]_1$ state to the $(^2P_{1/2})5f[5/2]_2$ autoionizing state is also a core-switching transition. The core-switching transitions must gain their strength from either configuration interaction in the bound state (so that the intermediate state contains character of states with both the $^2P_{3/2}$ and $^2P_{1/2}$ ion cores), or through configuration interaction in the continuum. To predict the branching ratios for the two ion states, the photoionization matrix elements for each of the interacting states are also required. Thus, even weak configuration interactions can result in a large effect on the branching ratio if the photoionization matrix elements have significantly different values, or if there is interference among the operative ionization channels. While the calculation of these cross sections is beyond the scope of the present work, some sense of the degree of interactions amongst the intermediate states can be obtained from the multichannel quantum defect theory study of Aymar et al.[32] In particular, Figure 3 of Ref. [32] shows the Lu-Fano plot for the $J = 1$ bound states of Kr. States that lie on the horizontal or vertical parts of this plot are relatively free from perturbations, while states that lie on the curved portions are more strongly mixed. Interestingly, none of the states of interest here lie on isolated horizontal or vertical sections of the plot, and the $(^2P_{3/2})5d[1/2]_1$ state (which shows strong core switching) looks to be significantly perturbed.

The effects of these perturbations are also expected to be seen in the PADs. For all of the intermediate states, Table III shows that the PADs are more anisotropic (i.e., larger magnitude c_2 and c_4 parameters) for the $^2P_{1/2}$ photoelectron band, regardless of whether the formation of this state requires a change in the value of J_c. In addition, the c_4 parameter has a significant magnitude for all of the observed PADs, regardless of the value of l or J_c, but is always larger for the core switching PAD than for the equivalent core conserving PAD. We note that while the PADs for the $^2P_{1/2}$ ion state look much like the PAD expected for a p electron at first glance, the contribution from the c_4 parameter causes a substantial narrowing of the PADs. Finally, for the $(^2P_{1/2})6s[1/2]_1$ intermediate state, the $\Delta l = \pm 1$ selection rule limits the photoelectron wavefunction to partial waves with $l = 1$. Thus, the observation of non-zero c_4 parameters in the corresponding PADs is somewhat surprising. However, configuration interaction with both $(^2P_{3/2})nd$ and $(^2P_{1/2})nd$ Rydberg states would open up the f-photoelectron continua as well, which likely accounts for the significant c_4 values.

4.3 Intermediate states that are indirectly populated

Eight photoelectron peaks are observed that are not consistent with one-photon ionization of the resonance that has been prepared. The corresponding photoelectron kinetic energies are listed in Table IV, along with plausible assignments of the excited state that gives rise to them. We have identified six excited states in total, these are: $(^2P_{3/2})6p[1/2]_1$, $(^2P_{1/2})5p[1/2]_1$, $(^2P_{3/2})6p[5/2]_{2,3}$, $(^2P_{3/2})4d[7/2]_3$, $(^2P_{3/2})4d[3/2]_2$ and $(^2P_{3/2})4d[1/2]_1$. If these states are populated by one-step, one-photon fluorescence from the initially prepared $J = 1$ state, which has odd parity, they must have even parity and $J = 0, 1, 2$. However, several of the states listed in Table III have odd parity: $(^2P_{3/2})4d[7/2]_3$, $(^2P_{3/2})4d[3/2]_2$, and $(^2P_{3/2})4d[1/2]_1$, and the first of these also has $J = 3$. There are two potential explanations for the appearance of these states: (i) They could be populated by a cascade of two sequential fluorescence events, providing that the final state lives sufficiently long to be ionized by the laser photon. This scenario is possible due to the continuous wave nature of the probe laser. (ii) They could result from the excitation and predissociation of Kr_2 or larger clusters in the molecular beam and subsequent ionization of the excited fragments. Such processes have been observed in the multiphoton ionization photoelectron spectroscopy of rare gas molecules.[33] Analysis of the ion time-of-flight data indicates that signal from the dimer is approximately 1% of the signal from the monomer, but could be somewhat higher due to dissociative ionization of the dimer above the monomer threshold. Although several factors would contribute to the intensity of features from such a predissociation process (including the relative transition probabilities to the low-lying Rydberg states of the monomer and dimer, the predissociation branching fraction, and the fragment photoionization cross section), the dimer concentration does not appear to be sufficient for this process to account for the intensity of the extra peaks observed in the photoelectron spectra. Therefore we believe that the extra peaks result from the ionization of fluorescently populated levels. The values of the c_L parameters for each of the extra peaks are listed in Table IV. The PADs (Fig. 8) for these features are generally less anisotropic than those shown in Fig. 7, as expected given the less restrictive selection rule controlling M_J in emission. We note that the only PAD to show a negative c_2 value is the one that involves a core switching transition, i.e., ionization of the $(^2P_{1/2})5p[1/2]_1$ state to give the $^2P_{3/2}$ ion state.

5. Conclusion

Kr atoms have been prepared in a series of selected intermediate resonances with synchrotron radiation and ionized with visible laser radiation. The spin-orbit state of both the ionized neutral Kr atoms and the resulting Kr^+ ions is observed to have a significant effect on the anisotropy of the ejected photoelectrons, whereas orbital angular momentum has a surprisingly small effect. The anisotropy, which is enhanced as a consequence of the two-photon scheme, also shows a strong

polarization dependence. There is evidence that electronic states populated through fluorescence are also photoionized, with the resulting PADs showing reduced anisotropy.

Acknowledgments

References

1. G. Wu, P. Hockett and A. Stolow, Phys. Chem. Chem. Phys. **13**, 18447-18467 (2011).

2. K. L. Reid, Annu. Rev. Phys. Chem. **54**, 397-424 (2003).

3. T. Seideman, J. Chem. Phys. **113**, 1677-1680 (2000).

4. E. Surber, R. Mabbs and A. Sanov, J. Phys. Chem. A **107**, 8215-8224 (2003).

5. D. J. Goebbert, K. Pichugin and A. Sanov, J. Chem. Phys. **131**, 164308 (2009).

6. T. Suzuki, L. Wang and H. Kohguchi, J. Chem. Phys. **111**, 4859-4861 (1999).

7. M. Tsubouchi, B. J. Whitaker, L. Wang, H. Kohguchi and T. Suzuki, Phys. Rev. Lett. **86**, 4500-4503 (2001).

8. P. Hockett, C. Z. Bisgaard, O. J. Clarkin and A. Stolow, Nature Phys. **7**, 612-615 (2011).

9. O. Gessner, A. M. D. Lee, J. P. Shaffer, H. Reisler, S. V. Levchenko, A. I. Krylov, J. G. Underwood, H. Shi, A. L. L. East, D. M. Wardlaw, E. T. Chrysostom, C. C. Hayden and A. Stolow, Science **311**, 219-222 (2006).

10. C. Z. Bisgaard, O. J. Clarkin, G. R. Wu, A. M. D. Lee, O. Gessner, C. C. Hayden and A. Stolow, Science **323**, 1464-1468 (2009).

11. J. A. Davies, R. E. Continetti, D. W. Chandler and C. C. Hayden, Phys. Rev. Lett. **84**, 5983-5986 (2000).

12. O. C. Mullins, R. L. Chien, J. E. Hunter, J. S. Keller and R. S. Berry, Phys. Rev. A **31**, 321-328 (1985).

13. G. Leuchs, S. J. Smith, E. Khawaja and H. Walther, Opt. Commun. **31**, 313-316 (1979).

14. Z. M. Wang and D. S. Elliott, Phys. Rev. A **62**, 053404 (2000).

15. B. Doughty, L. H. Haber, C. Hackett and S. R. Leone, J. Chem. Phys. **134**, 094307 (2011).

16. F. J. Wuilleumier and M. Meyer, J. Phys. B-Atomic Molecular and Optical Phys. **39**, R425-R477 (2006).

17. M. Meyer, Nucl. Instrum. Methods Phys. Res. A **601**, 88-97 (2009).

18. P. O'Keeffe, P. Bolognesi, A. Mihelic, A. Moise, R. Richter, G. Cautero, L. Stebel, R. Sergo, L. Pravica, E. Ovcharenko, P. Decleva and L. Avaldi, Phys. Rev. A **82**, 052522 (2010).

19. P. O'Keeffe, E. V. Gryzlova, D. Cubaynes, G. A. Garcia, L. Nahon, A. N. Grum-Grzhimailo and M. Meyer, Phys. Rev. Lett. **111**, 243002 (2013).

20. E. V. Gryzlova, P. O'Keeffe, D. Cubaynes, G. A. Garcia, L. Nahon, A. N. Grum-Grzhimailo and M. Meyer, New J. Phys. **17**, 043054 (2015).

21. L. Nahon, N. de Oliveira, G. A. Garcia, J.-F. Gil, B. Pilette, O. Marcouille, B. Lagarde and F. Polack, J. Synchr. Rad. **19**, 508-520 (2012).

22. X. Tang, G. A. Garcia, J.-F. Gil and N. L., Rev. Sci. Instrum. **86**, 123108 (2015).

23. G. A. Garcia, B. K. C. de Miranda, M. Tia, S. Daly and L. Nahon, Rev. Sci. Instrum. **84**, 053112 (2013).

24. E. B. Saloman, J. Phys. and Chem. Reference Data **36**, 215-386 (2007).

25. L. Nahon and C. Alcaraz, Appl. Opt. **43**, 1024-1037 (2004).

26. G. A. Garcia, L. Nahon and I. Powis, Rev. Sci. Instrum. **75**, 4989-4996 (2004).

27. G. Racah, Phys. Rev. **61**, 537-539 (1942).

28. R. L. Dubs, S. N. Dixit and V. McKoy, Phys. Rev. Lett. **54**, 1249-1251 (1985).

29. M. P. Strand, J. Hansen, R. L. Chien and R. S. Berry, Chem. Phys. Lett. **59**, 205-209 (1978).

30. V. A. Shubert and S. T. Pratt, Phys. Rev. A **84**, 053413 (2011).

31. V. L. Sukhorukov, I. D. Petrov, M. Schaefer, F. Merkt, M. W. Ruf and H. Hotop, J. Phys. B **45**, 092001 (2012).

32. M. Aymar, O. Robaux and C. Thomas, J. Phys. B **14**, 4255 (1981).

33. S. T. Pratt, P. M. Dehmer and J. L. Dehmer, Chem. Phys. Lett. **116**, 245-249 (1985).

Table I: The intermediate electronic states prepared by the synchrotron radiation

VUV photon energy / eV	Kr state accessed
12.03703	$(^2P_{3/2})4d[1/2]_1$
12.86978	$(^2P_{3/2})5d[1/2]_1$
13.00437	$(^2P_{1/2})4d[3/2]_1$
13.03648	$(^2P_{1/2})6s[1/2]_1$
13.09874	$(^2P_{3/2})5d[3/2]_1$

Table II: Anisotropy parameters for ionization of the $(^2P_{3/2})4d[1/2]_1$ resonance as a function of energy. See Section 3 for a discussion of error bars.

LP-LP				
laser wavelength (nm)	total energy (eV)	electron kinetic energy (eV)	c_2	c_4
596.341	14.11611	0.11651	0.44	-1.28
596.040	14.11716	0.11756	0.28	-1.11
595.987	14.11735	0.11775	0.60	-0.99
595.929	14.11755	0.11795	0.74	-0.79
595.920	14.11758	0.11798	0.81	-0.21
595.903	14.11764	0.11804	0.86	0.04
595.671	14.11845	0.11885	0.84	-0.38

Circular Polarization			RCP,LCP		RCP,RCP	
laser wavelength (nm)	total energy (eV)	electron kinetic energy (eV)	c_2	c_4	c_2	c_4
600.040	14.10330	0.10370	0.21	-0.35	-0.5	-0.13
600.011	14.10340	0.10380	0.17	-0.36	-0.63	-0.07
595.966	14.11742	0.11782	0.17	-0.67	-0.54	-0.15
595.915	14.11760	0.11800	0.10	-0.56	-0.78	-0.04
595.876	14.11773	0.11813	0.19	-0.29	-0.87	-0.03

Table III: Anisotropy parameters and spin-orbit branching ratios for direct ionization of the $(^2P_{3/2})5d[1/2]_1$, $(^2P_{1/2})4d[3/2]_1$, $(^2P_{1/2})6s[1/2]_1$ and $(^2P_{3/2})5d[3/2]_1$ resonances. The branching ratios are determined by integrating under the relevant peaks in the photoelectron spectra. See Section 3 for a discussion of error bars.

resonance	Polarization	Spin-orbit state	Branching ratio	c_2	c_4
$(^2P_{3/2})5d[1/2]_1$	(LP,LP)	$^2P_{3/2}$	0.3	0.64	-0.69
		$^2P_{1/2}$	0.7	1.72	1.07
	(RCP,LCP)	$^2P_{3/2}$	0.5	0.01	-0.23
		$^2P_{1/2}$	0.5	-0.53	0.70
	(RCP,RCP)	$^2P_{3/2}$	0.4	-0.62	-0.05
		$^2P_{1/2}$	0.6	-1.11	0.13
$(^2P_{1/2})4d[3/2]_1$	(LP,LP)	$^2P_{3/2}$	0.3	0.46	-1.06
		$^2P_{1/2}$	0.7	1.57	1.22
$(^2P_{1/2})6s[1/2]_1$	(LP,LP)	$^2P_{3/2}$	0.7	0.25	-1.22
		$^2P_{1/2}$	0.3	1.82	0.86
$(^2P_{3/2})5d[3/2]_1$	(LP,LP)	$^2P_{3/2}$	0.8	2.41	0.61
		$^2P_{1/2}$	0.2	2.42	1.17

Table IV: Photoelectron kinetic energies and anisotropy parameters observed following ionization of the fluorescently populated states (see text and Fig. 6). See Section 3 for a discussion of error bars.

Intermediate resonance prepared	Observed eke / eV	Assigned transition $\lvert i\rangle \rightarrow \lvert f\rangle$	Expected eke / eV	c_2	c_4
$(^2P_{1/2})4d[3/2]_1$	0.844	$(^2P_{3/2})6p[1/2]_1 \rightarrow (^2P_{3/2})$	0.841	0.69	0.35
	0.223	$(^2P_{1/2})5p[1/2]_1 \rightarrow (^2P_{3/2})$	0.225	-0.07	-0.23
$(^2P_{1/2})6s[1/2]_1$	0.844	$(^2P_{3/2})6p[1/2]_1 \rightarrow (^2P_{3/2})$	0.841	0.70	-0.15
	0.224	$(^2P_{1/2})5p[1/2]_1 \rightarrow (^2P_{3/2})$	0.225	0.06	0.08
$(^2P_{3/2})5d[3/2]_1$	0.868	$(^2P_{3/2})6p[5/2]_{2,3} \rightarrow (^2P_{3/2})$	0.870	0.98	0.34
	0.259	$(^2P_{3/2})4d[7/2]_3 \rightarrow (^2P_{3/2})$	0.263	0.99	0.34
	0.200	$(^2P_{3/2})4d[3/2]_2 \rightarrow (^2P_{3/2})$	0.196	0.51	-0.09
	0.117	$(^2P_{3/2})4d[1/2]_1 \rightarrow (^2P_{3/2})$	0.121	0.38	0.18

Table V: Allowed Ionization Continua for Photoionization of Selected Levels of Kr.

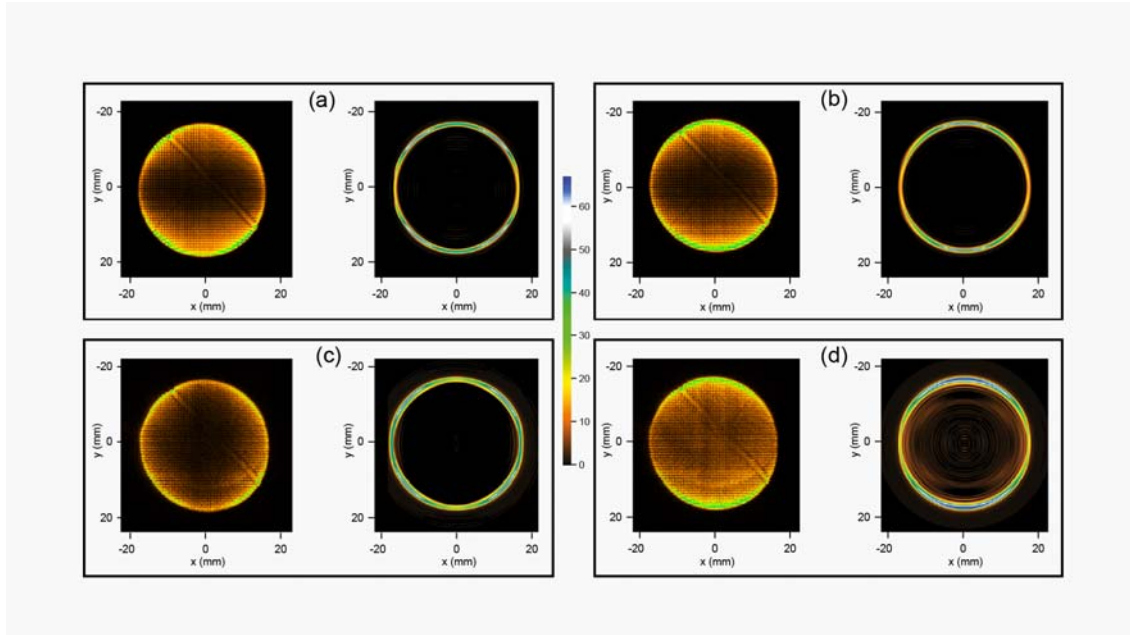| Intermediate State	$(^2P_{J_c})\epsilon l$	$[K]_J$		
		LP,LP $M_J = 0\to0$	RCP,RCP $M_J = 1\to2$	RCP,LCP $M_J = 1\to0$
$(^2P_{3/2})5d[1/2]_1$ $(^2P_{1/2})4d[3/2]_1$ $(^2P_{3/2})5d[3/2]_1$	$(^2P_{3/2})\epsilon p$	$[1/2]_0$		$[1/2]_0$
				$[1/2]_1$
				$[3/2]_1$
		$[3/2]_2$	$[3/2]_2$	$[3/2]_2$
		$[5/2]_2$	$[5/2]_2$	$[5/2]_2$
	$(^2P_{3/2})\epsilon f$			$[3/2]_1$
		$[3/2]_2$	$[3/2]_2$	$[3/2]_2$
		$[5/2]_2$	$[5/2]_2$	$[5/2]_2$
	$(^2P_{1/2})\epsilon p$	$[1/2]_0$		$[1/2]_0$
				$[1/2]_1$
				$[3/2]_1$
		$[3/2]_2$	$[3/2]_2$	$[3/2]_2$
	$(^2P_{1/2})\epsilon f$	$[5/2]_2$	$[5/2]_2$	$[5/2]_2$
$(^2P_{1/2})6s[1/2]_1$	$(^2P_{3/2})\epsilon p$	$[1/2]_0$		$[1/2]_0$
				$[1/2]_1$
				$[3/2]_1$
		$[3/2]_2$	$[3/2]_2$	$[3/2]_2$
		$[5/2]_2$	$[5/2]_2$	$[5/2]_2$
	$(^2P_{1/2})\epsilon p$	$[1/2]_0$		$[1/2]_0$
				$[1/2]_1$
				$[3/2]_1$
		$[3/2]_2$	$[3/2]_2$	$[3/2]_2$

Figures

Fig. 1 Raw (left image in each panel) and inverted (right image in each panel) photoelectron images following the photoexcitation of Kr atoms to the $(^2P_{3/2})4d[1/2]_1$ state and photoionization with visible laser light of wavelength λ in different polarization geometries. (a) λ = 595.929 nm, (LP,LP); (b) λ = 595.920 nm, (LP,LP); (c) λ = 595.915 nm, (RCP,LCP); (d) λ = 595.915 nm, (RCP,RCP). The inverted images have been processed such that only electrons measured in coincidence with Kr atoms with zero nuclear spin are included. The cylindrical symmetry axis (polarization vector for LP, propagation axis for RCP/LCP) points vertically in all cases.
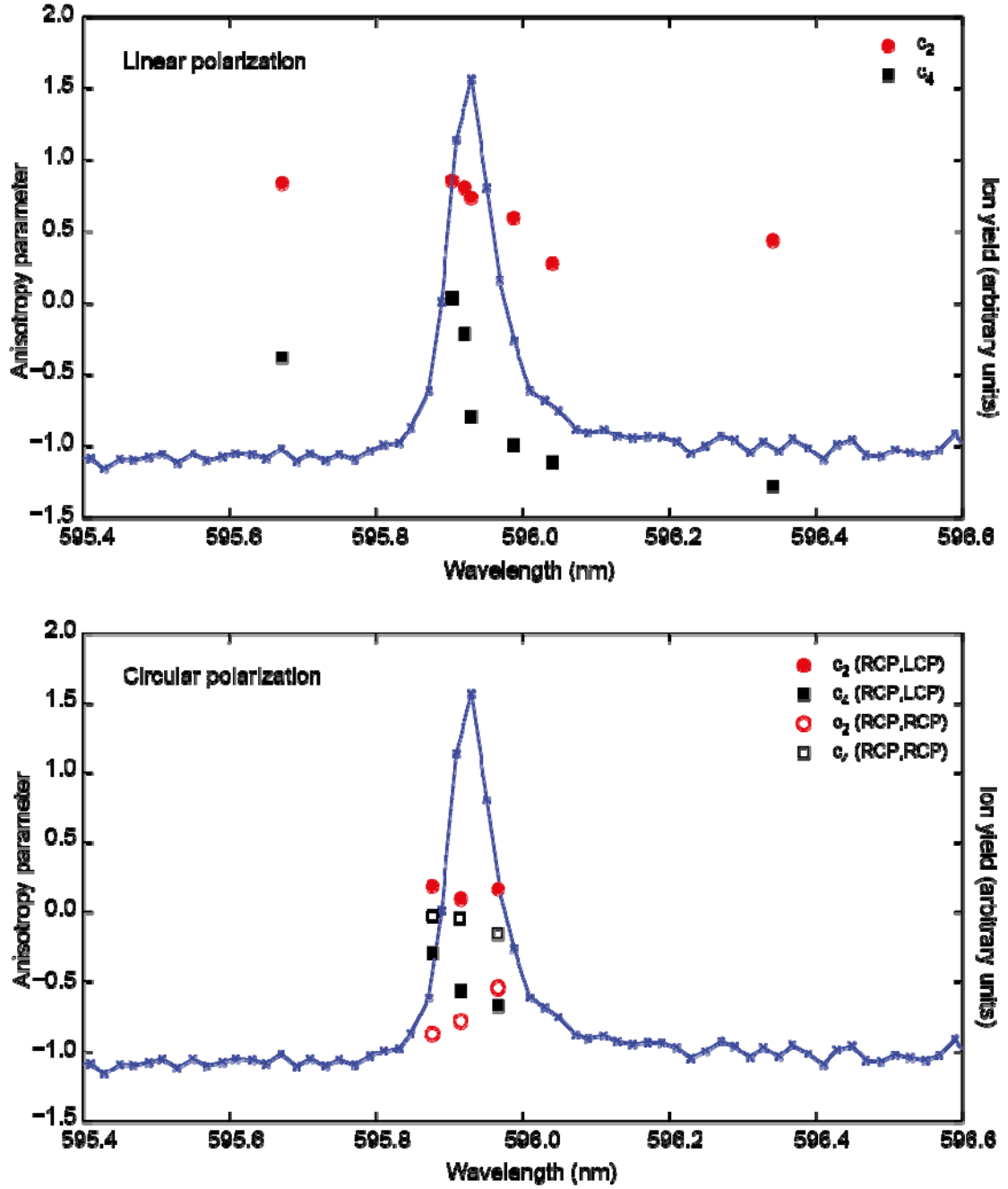
Fig. 2 Ion yield and photoelectron anisotropy parameters as a function of the wavelength used to ionize the prepared $(^{2}P_{3/2})4d[1/2]_1$ state in Kr isotopes with zero nuclear spin in the (LP,LP) geometry (upper panel) and in the two CP geometries (lower panel). The c_2 parameters are given as red circles and the c_4 parameters as black squares; see Eq. (5). In the lower panel filled symbols indicate (RCP,LCP) and open symbols indicate (RCP,RCP).
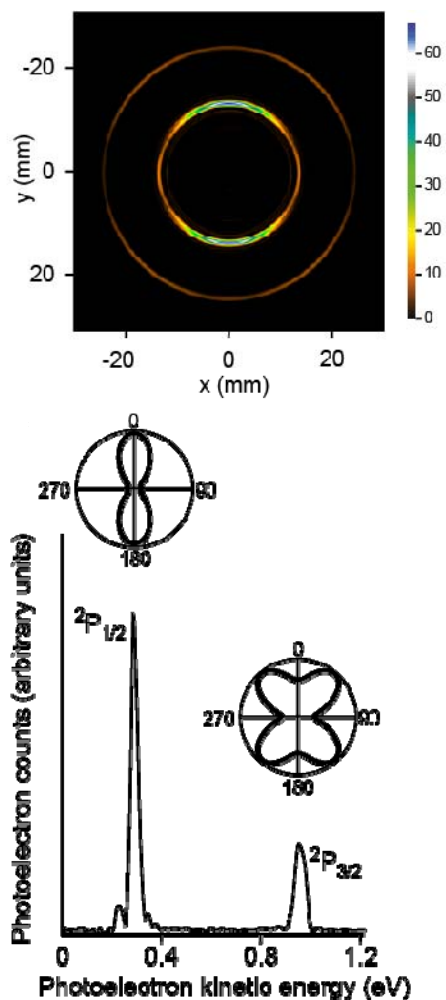
Fig. 3 Top: Inverted photoelectron image following excitation of the $(^2P_{3/2})5d[1/2]_1$ state in Kr isotopes with zero nuclear spin, and ionization with 595 nm in the (LP,LP) geometry. Bottom: The photoelectron spectrum as a function of the photoelectron kinetic energy. Middle: Polar plots of photoelectron intensity corresponding to the two Kr^+ spin-orbit states formed. The vertical axis is aligned with the direction of the linear polarization vector.
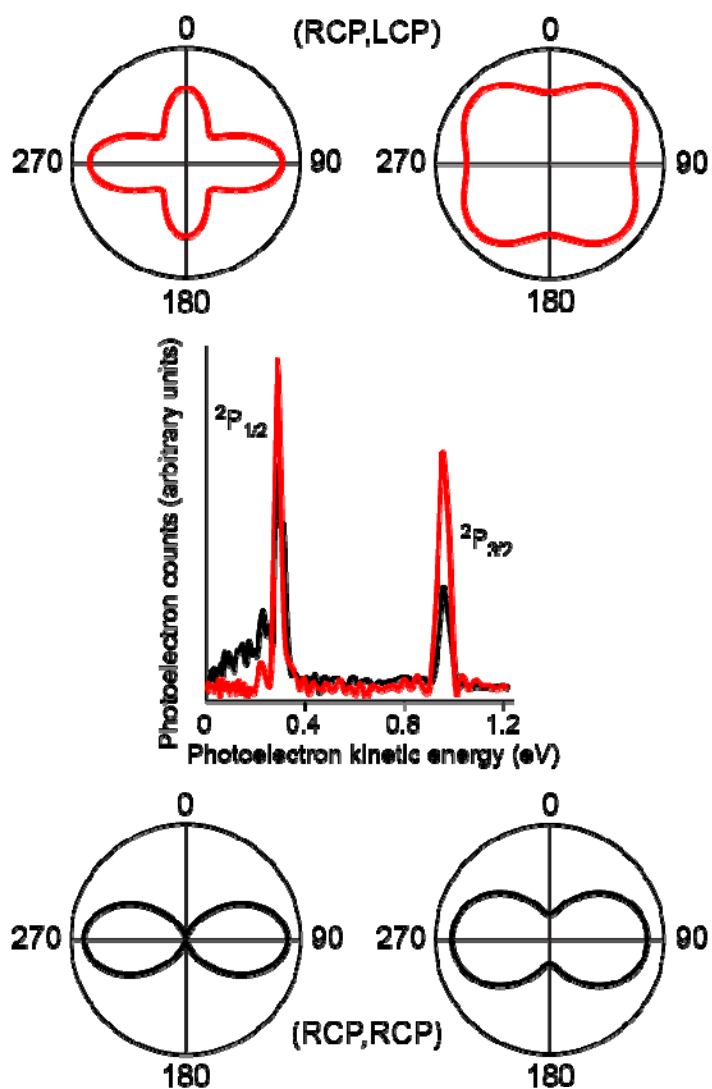
Fig. 4 Photoelectron spectra and PADs (polar plots of photoelectron intensity) extracted from photoelectron images measured following excitation of the $(^2P_{3/2})5d[1/2]_1$ state in Kr isotopes with zero nuclear spin, and ionization with 595 nm in the (RCP,RCP) (black) and (RCP,LCP) (red) geometries. The two spectra are normalized to each other at the peak of the $^2P_{1/2}$ feature. The PADs correspond to formation of the Kr^+ ion in its $^2P_{1/2}$ state (left) and its $^2P_{3/2}$ state (right). The vertical axis is aligned with the direction of laser light propagation.
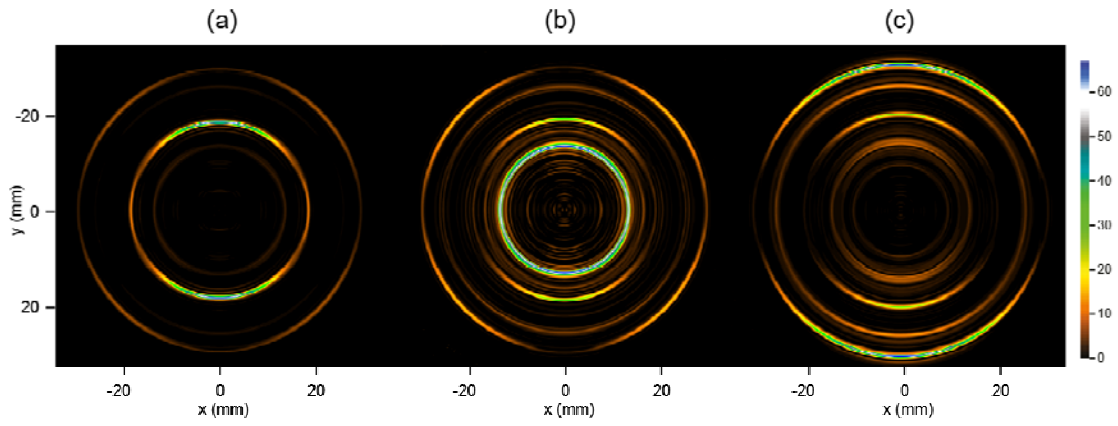
Fig. 5 Inverted photoelectron images measured in the (LP,LP) geometry following excitation of (a) ($^2P_{1/2}$)4d[3/2]$_1$, (b) ($^2P_{1/2}$)6s[1/2]$_1$ and (c) ($^2P_{3/2}$)5d[3/2]$_1$ in Kr isotopes with zero nuclear spin and ionization with 595 nm. The vertical axis is aligned with the direction of the linear polarization vector.
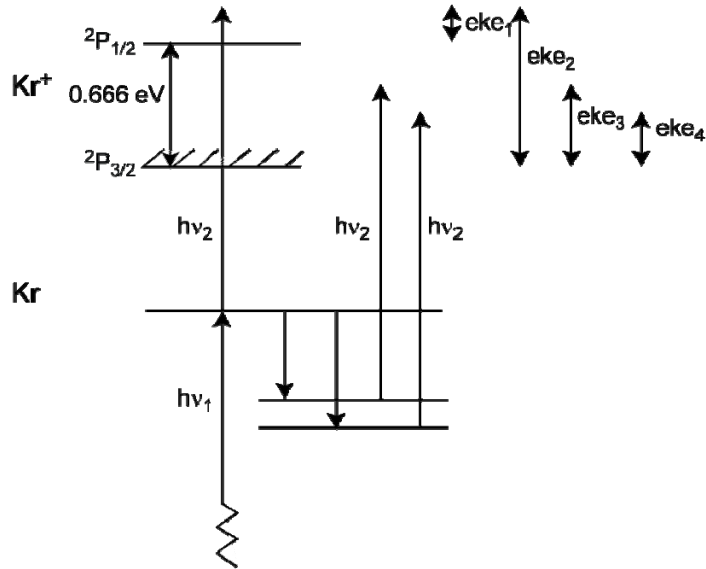

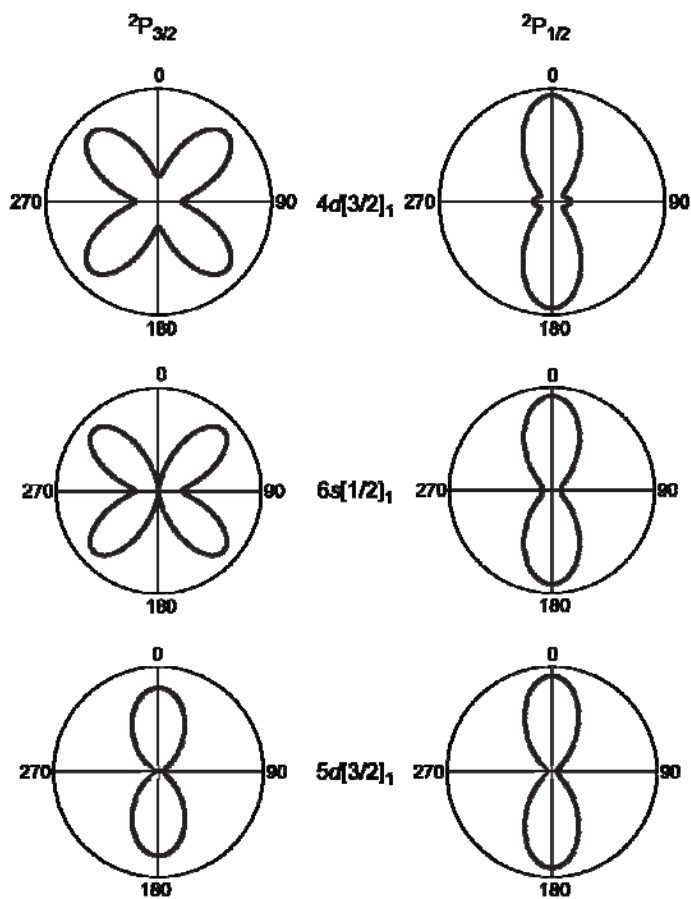Fig. 6 Scheme explaining the multiple rings observed in the images shown in Fig. 5.

Fig. 7 Polar plots of photoelectron intensity following ionization of the (^{2}P$_{1/2}$)4d[3/2]$_1$, (^{2}P$_{1/2}$)6s[1/2]$_1$, and (^{2}P$_{3/2}$)5d[3/2]$_1$ intermediate states with zero nuclear spin (top to bottom), and ionization with 595 nm light in the (LP,LP) geometry to form the two Kr$^+$ spin-orbit states (left and right). The vertical axis is aligned with the direction of the linear polarization vector.
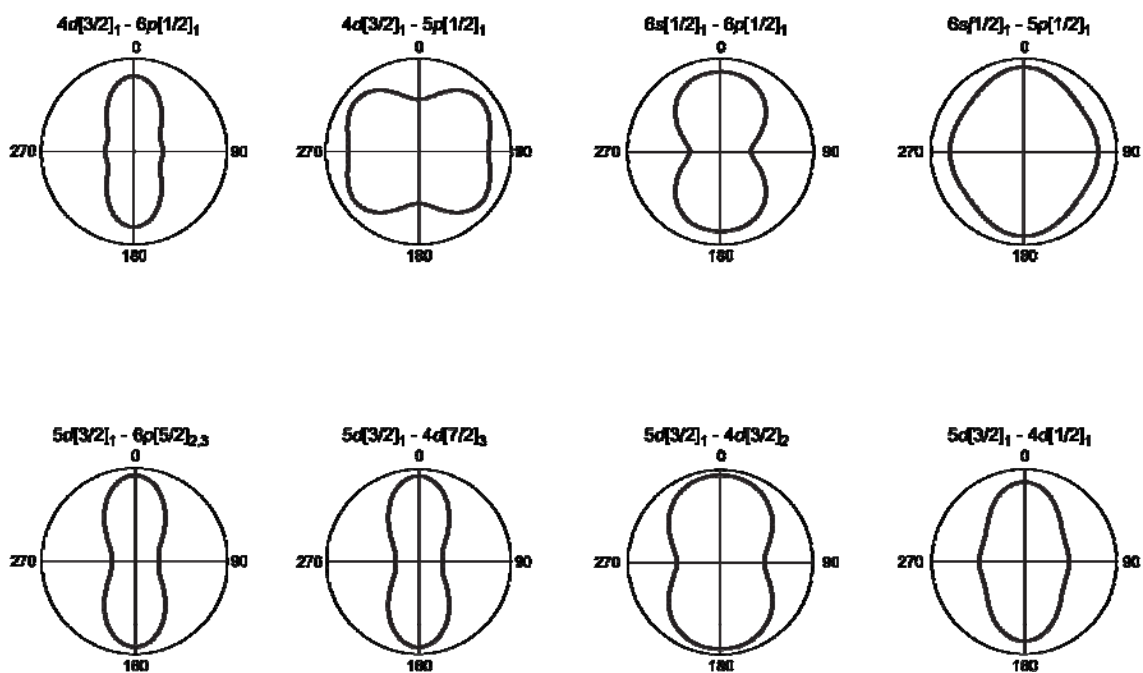
Fig. 8 Polar plot of photoelectron intensity following the ionization of electronic states populated through fluorescence. The fluorescing transition is labelled in each case, with the first state being the one prepared by the SR. The (LP,LP) geometry was used for the initial excitation/ionization scheme. In all cases Kr$^+$ is formed in its ground spin-orbit state ($^2P_{3/2}$). The vertical axis is aligned with the direction of the linear polarization vector.